Numerical modeling of protocore destabilization during planetary accretion: Methodology and results

Ja-Ren Lin [a,b,*], Taras V. Gerya [b], Paul J. Tackley [b], David A. Yuen [c], Gregor J. Golabek [b]

[a] Institute of Oceanography, National Taiwan University, Taiwan
[b] Geophysical Fluid Dynamics Group, Institute of Geophysics, Department of Geosciences, ETH-Zurich, Switzerland
[c] University of Minnesota Supercomputing Institute, Department of Geology and Geophysics, University of Minnesota, Minneapolis, MN55455, USA

ARTICLE INFO

ABSTRACT

We developed and tested an efficient 2D numerical methodology for modeling gravitational redistribution processes in a quasi spherical planetary body based on a simple Cartesian grid. This methodology allows one to implement large viscosity contrasts and to handle properly a free surface and self-gravitation. With this novel method we investigated in a simplified way the evolution of gravitationally unstable global three-layer structures in the interiors of large metal–silicate planetary bodies like those suggested by previous models of cold accretion [Sasaki, S., Nakazawa, K., 1986. J. Geophys. Res. 91, 9231–9238; Karato, S., Murthy, V.R., 1997. Phys. Earth Planet Interios 100, 61–79; Senshu, H., Kuramoto, K., Matsui, T., 2002. J. Geophys. Res. 107 (E12), 5118. 10.1029/2001JE001819]: an innermost solid protocore (either undifferentiated or partly differentiated), an intermediate metal-rich layer (either continuous or disrupted), and an outermost silicate-rich layer. Long-wavelength (degree-one) instability of this three-layer structure may strongly contribute to core formation dynamics by triggering planetary-scale gravitational redistribution processes. We studied possible geometrical modes of the resulting planetary reshaping using scaled 2D numerical experiments for self-gravitating planetary bodies with Mercury-, Mars- and Earth-size. In our simplified model the viscosity of each material remains constant during the experiment and rheological effects of gravitational energy dissipation are not taken into account. However, in contrast to a previously conducted numerical study [Honda, R., Mizutani, H., Yamamoto, T., 1993. J. Geophys. Res. 98, 2075–2089] we explored a freely deformable planetary surface and a broad range of viscosity ratios between the metallic layer and the protocore (0.001–1000) as well as between the silicate layer and the protocore (0.001–1000). An important new prediction from our study is that realistic modes of planetary reshaping characterized by a high viscosity protocore and low viscosity molten silicate and metal [Senshu, H., Kuramoto, K., Matsui, T., 2002. J. Geophys. Res. 107 (E12), 5118. 10.1029/2001JE001819] may result in the transient exposure of the protocore to the planetary surface and a strongly (up to 8% of the planetary diameter) aspherical deviation of the planetary shape during the early stages of core formation. Exposure of the protocore might happen in the early stages of iron core formation. This process may conceivably convert a large amount of potential energy into temperature increase and a transient strongly non-uniform depth of the magma ocean around the protoplanet. Our simplified model also predicts that the time for metallic core formation out of the metal-rich layer depends mainly on the dynamics of the deformation of the solid strong protocore. In nature this dynamics will be strongly dependent on the effective viscosity of the protocore, which should generally have non-Newtonian pressure-, temperature-, and stress-dependent rheology with strong thermomechanical feedbacks from gravitational energy dissipation.

© 2009 Elsevier Inc. All rights reserved.

1. Introduction

The core formation of the terrestrial bodies is one of the most important but poorly understood problems in geosciences. There is still no consensus on the process of core formation, which involves the separation of iron-rich material from silicates and its migration to the center of the protoplanet. Core formation and planetary accretion in the terrestrial zone are intimately linked.

* Corresponding author. Address: Institute of Oceanography, National Taiwan University, No. 1, Sec. 4, Roosevelt Rd., Taipei 10617, Taiwan.
 E-mail addresses: linj@erdw.ethz.ch (J.-R. Lin), taras.gerya@erdw.ethz.ch (T.V. Gerya), ptackley@ethz.ch (P.J. Tackley), daveyuen@gmail.com (D.A. Yuen), gregor.golabek@erdw.ethz.ch (G.J. Golabek).

The accretion history strongly controlled the composition and the thermal state of the growing planetary embryos. Terrestrial planets are thought to have grown through several stages. At first, km-sized bodies called planetesimals were formed from the dusty protoplanetary disk. This stage was followed by the accretion of planetesimals into Mars-sized planetary embryos by runaway growth. During the next stage, the oligarchic growth, the planetary embryos fed on material in their respective feeding zones. Finally the embryos perturbed each others orbits, which led to the formation of Earth-sized planets by giant impacts between planetary embryos. The first two stages was very short (∼1 Myr) and the last stage was on the order of 100 Myr (Chambers, 2004). These results suggest a relatively hot planetary interior due to impacts and decay of short-lived radioactive isotopes.

However, results by Wetherill (1992), Grimm and McSween (1993), and Raymond et al. (2007) indicate that the accretion rate is dependent on the radial distance from the Sun. Therefore we may expect longer accretion timescales in the outer regions of the terrestrial zone, which corresponds to the present Asteroid belt. Numerical models indicate that this region is today highly depleted (e.g., O'Brien et al., 2007) in mass (>99.9% of the initial mass is missing (Chambers and Wetherill, 2001)) due to gravitational scattering by the early formed gas giants (e.g., Pollack et al., 1996). Numerical N body simulations (Chambers and Wetherill, 1998, 2001; O'Brien et al., 2007) confirm that Moon-to Mars-sized bodies could have accreted in this region as was first suggested by Wetherill (1992). According to these simulations, planetary embryos are driven out of the Asteroid belt on timescales ranging from tens to hundreds of Ma. They are ejected from the system, hit the Sun or are accreted into the forming terrestrial planets.

Therefore it seems feasible that these bodies could have accreted cold as the efficiency of radioactive heating by short-lived radioactive isotopes like ^{26}Al and ^{60}Fe is highly dependent on the accretion time of a planetary body (e.g. Merk et al., 2002). Core formation on such bodies could therefore be delayed and start at the latest when the growing planetary embryos reached Mars mass, as impacts were then energetic enough to cause significant melting (Melosh, 1990; Senshu et al., 2002) near the surface. This is feasible as the average size of accreting bodies increased with time (e.g. Wetherill, 1990). Results from Earth differentiation models neglecting short-lived radioactive heating sharing the assumption of cold accretion might therefore be applied on this scenario. Basically these models suggest that a three-layered structure develops (Sasaki and Nakazawa, 1986; Honda et al., 1993; Karato and Murthy, 1997; Senshu et al., 2002). On top they predict a silicate layer, possibly an impact-induced magma ocean. The metal–silicate separation occurred in this magma ocean through cm-sized iron droplets sinking through liquid silicates and a dense iron layer was formed by sedimentation of the iron droplets on the base of the magma ocean (Rubie et al., 2003; Hoink et al., 2006). The inner region would still consist of a cold undifferentiated mixture of iron and silicate material and present a viscosity jump owing to the crystallization of the magma ocean (Karato and Murthy, 1997; Solomatov, 2000). The beginning of crystallization of the magma oceans depends on the poorly known thermal state of the mantle (Solomatov, 2000), which was affected by the accretion rate and the thermal state of the accreted bodies (either differentiated or undifferentiated or a mixture of them, Rubie et al., 2007), and could further influence the evolution of the iron layer and the mechanisms of core formation.

Iron diapirs have been proposed to sink through the viscous silicate mantle (Elsasser, 1963; Karato and Murthy, 1997; Samuel and Tackley, 2008), or through stress-induced channels (Golabek et al., 2008), to the center of the protoplanet. This degree $L \geqslant 2$ scenario is preferred for the forming terrestrial planets as a high temperature accretion is expected, which ensures a low viscosity of the solid regions. However in the discussed scenario of cold accretion we have to assume that due to the low temperatures inside the protoplanet the viscosity of the central region is high. Stevenson (1981) and Ida et al. (1987) proposed the $L = 1$ mode of core formation for such a scenario, in which the central region of the planetary embryo is pushed outwards due to an asymmetry in the iron layer thickness, which leads to the defragmentation of the protocore. Impacts are likely to destabilize the iron layer.

The instability of a global iron-rich layer was investigated analytically by Ida et al. (1987) with two layers, an iron layer and an undifferentiated protocore. They confirmed that the $L = 1$ mode suggested by Stevenson's (1981) process is the fastest mode of the instability (Degree $L = 1$ mode in the Rayleigh–Taylor instability), which can occur on timescales as short as 10 h. Ida et al. (1989) showed that in a two-layered system the time scale for the core formation depends on the dominant Rayleigh–Taylor instability mode and the viscosity contrast between the layers. For the $L = 1$ mode, corresponding to the case when the non-deforming protocore is displaced within the deforming iron layer, this time scale is determined by the viscosity of the iron layer. For $L \geqslant 2$ modes, for which both the iron layer and the protocore are deformed, this timescale is determined by the viscosity of the strongest material. The time scale becomes longer as the angular order of the unstable mode increases.

Honda et al. (1993) first investigated this scenario using a numerical model of the flow field in a self-gravitating three-layered fluid sphere, the outermost silicate layer, the iron-rich layer, and the undifferentiated core. Their results showed that the mechanism of core formation is dependent on the viscosity of the protocore. For a protocore viscosity greater than 10^{26} Pa s a single iron diapir of several thousand kilometers size is formed. Subsequently, the center position is replaced by the newly formed iron core. This picture is similar to the proposal of Elsasser (1963). For lower viscosities of the central region several smaller diapirs may be extracted from the iron layer and form the iron core gradually.

The numerical study of Honda et al. (1993) assumed a non-deformable planetary surface and no viscosity contrast between the solid protocore and the molten outer silicate layer, assumptions that limit the applicability of their model to natural cases. As has been demonstrated by Gerya and Yuen (2007), internal reshaping of the planetary embryo during iron core formation (shell tectonics) will likely cause strong transient aspherical deviation of the initially spherical planetary surface, which should be taken into account in numerical experiments.

In this paper we develop and test a 2D numerical methodology for modeling gravitational redistribution processes in a planetary body based on a simple Cartesian grid. With this novel method we investigate in a simplified way the above mentioned tendency of forming gravitationally unstable global three-layer structures in the interiors of large metal–silicate planetary bodies with Mercury-, Mars- and Earth radii. In our simplified model the viscosity of each material remains constant during the experiment and rheological effects of gravitational energy dissipation are not taken into account. However, in contrast to the earlier numerical study by Honda et al. (1993), we explored a freely deformable planetary surface and a broad range of viscosity ratios between the metallic layer and the protocore (0.001–1000) as well as between the silicate layer and the protocore (0.001–1000). In Section 2 we provide the governing equations and the numerical methods used to solve them. Numerical accuracy tests and benchmarks of our numerical methodology are given in Section 3. Section 4 discusses results of systematic planetary reshaping modeling. Discussions and conclusions are given in Section 5.

2. Method of the simulation

2.1. Governing equations

We simulated in 2D a quasi spherical self-gravitating planetary body with a simplified gravitationally unstable three-layer structure, surrounded by a massless weak medium. We assume materials in the calculation are incompressible fluids, which are distinguished by the density and viscosity. Then the Lagrangian continuity equation for incompressible flow is

$$\vec{\nabla} \cdot \vec{u} = 0 \tag{1}$$

where $\vec{u}$ is the velocity. The equation of motion neglects the inertial term and reduces to

$$\vec{\nabla} \cdot \underline{\sigma} - \vec{\nabla} P = \rho \vec{\nabla} \Phi(x, z, t) \tag{2}$$

where σ is the deviatoric stress tensor, P is the pressure, Φ is the gravitational potential, which is time-dependent owing to the rearrangement of masses during the differentiation, and ρ is the density. It should be noticed that Eq. (2) has a steady state form, however, the actual fluid motion is not steady because the deformation of the protocore results in the redistribution of materials inside the planetary body that changes the density and gravity fields for every time step. We neglect the thermal buoyancy because the driving force from the compositional density difference between the metal and protocore is more important during core formation, which involves the overturn of materials inside the protoplanet. Thus, no heat equation is considered here. By considering self-gravitation, we combined a Poisson equation into our governing equations.

$$\nabla^2 \Phi = 4 K \pi \gamma \rho(x, z, t) \tag{3}$$

where γ is the gravitational constant, and K is a scaling factor for simulating a 3D spherical gravity field in 2D (Gerya and Yuen, 2007). We used $K = 2/3$ which scales a 2D gravity field inside a cylinder of a constant density ρ

$$\Phi(r)_{cylindrical} = \pi \gamma \rho r^2 \tag{4}$$

$$g(r)_{cylindrical} = -\frac{\partial \Phi(r)_{cylindrical}}{\partial r} = -2\pi \gamma \rho r \tag{5}$$

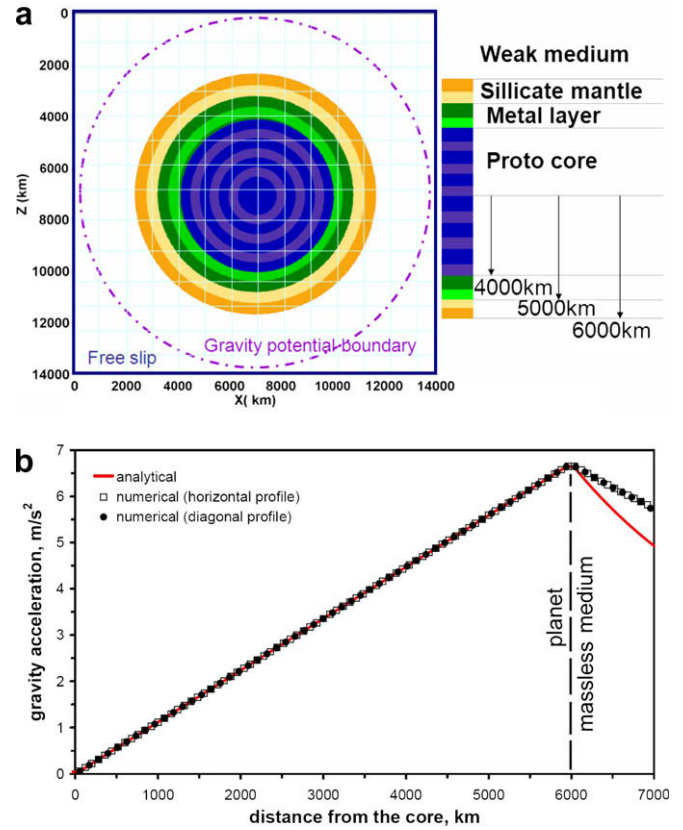to a 3D gravity field inside the sphere of the same density

$$\Phi(r)_{spherical} = \frac{2}{3} \pi \gamma \rho r^2 \tag{6}$$

$$g(r)_{spherical} = -\frac{\partial \Phi(r)_{spherical}}{\partial r} = -\frac{4}{3} \pi \gamma \rho r \tag{7}$$

where r is the distance from the center of the cylinder/sphere.

Obviously, this simplified scaling approach does not allow for the exact reproduction of a spherical gravity field and deformation in 2D. In particular, outside the planet gravitational acceleration is notably overestimated (Fig. 1b) since there it is proportional to $1/r^2$ for the spherical gravity field and to $1/r$ for the cylindrical one. However, as will be shown below by our benchmark, this approach correctly captures relative changes in the growth rates of a spherical $L = 1$ instability with changing model parameters, which is sufficient for the purpose of our simplified study and demonstrates that our new approach could serve as a tool box for more complex and realistic simulations.

In the present study we used a simplified Newtonian rheology for all materials in order to study the first-order geometrical variability of internal reshaping processes in the case of various three-layer planetary structures. Such systematic simplified modeling provides a necessary first step in the understanding of degree $L = 1$ instability before applying more complicated scenarios and

Fig. 1. Initial model set up used for numerical accuracy tests (a) and comparison of 1D analytical (Eq. (7)) and 2D numerical (Eq. (3)) solutions (along two different directions) for gravity field inside the spherical protoplanet of constant density of 4000 kg m^{-3}. The protoplanet in (a) is composed of three materials, which are silicate (bright and light yellow, $\rho = 4000$ kg m^{-3}, $d = 1000$ km), metal (dark and light green, $\rho = 10,060$ kg m^{-3}, $d = 1000$ km), and primitive material (blue and purple, $\rho = 5515$ kg m^{-3}, $r = 4000$ km). A weak medium (white, $\rho = 1$ kg m^{-3}) fills the remaining space. A free-slip mechanical boundary condition is applied on all boundaries. A constant gravitational potential condition is set on the internal circular boundary (dashed line) located at a distance from the protoplanet. (For interpretation of the references to color in this figure legend, the reader is referred to the web version of this article.)

material properties. The deviatoric stress components σ_{ij} in Eq. (1) are formulated from the viscous constitutive relationships

$$\sigma_{ij} = 2 \eta \dot{\varepsilon}_{ij} \tag{8}$$

$$\dot{\varepsilon}_{ij} = (\partial u_j / \partial x_i + \partial u_i / \partial x_j)/2 \tag{9}$$

where η is viscosity, $\dot{\varepsilon}_{ij}$ is strain rate, and u_i, u_j are components of velocity vector $\vec{u}$.

2.2. Numerical method and the boundary condition

The governing equations are solved by the finite-difference numerical code I2ELVIS, which uses a marker-in-cell technique for the advection of transport properties in a rectangular Cartesian staggered grid (Gerya and Yuen, 2007). Marker particles are employed to represent the distribution and movement of different materials, and the density of the marker grid in different experiments is varied from 4 to 400 per computational grid cell. The computational grid is uniform with a resolution varied from 141×141 to 301×301 nodal points in different cases.

The size of the model box depends on the protoplanet's radius in order to set a boundary condition for the gravitational potential, which is defined to be constant on the circular surface located at a given distance from the body (see the dashed line in Fig. 1a). In

choosing this type of boundary condition we used the tendency of gravity acceleration and gravity potential around a protoplanet to become a function of solely the distance r from the body's center when this distance is sufficiently large

$$g(r)_{spherical} = -\frac{\gamma M}{r^2} \tag{10}$$

$$\Phi(r)_{spherical} = \Phi(\infty)_{spherical} - \frac{\gamma M}{r} \tag{11}$$

where M is the mass of the protoplanet and $\Phi(\infty)_{spherical} = const$ is the gravitational potential at an infinite distance from the protoplanet. As we show below with our numerical test (4) in Section 3.1, convergence of the numerical solution is achieved with relatively small distances of the constant gravitational potential boundary from the surface of the body (cf. dashed line in Fig. 1a). This scaled 2D approach also allows for the correct reproduction of a spherical gravity field inside a protoplanet of constant density (Fig. 1b). Our numerical solution for the gravity field obtained on a Cartesian grid is direction independent (cf. horizontal and diagonal profiles in Fig. 1b), proving the validity of our spherical-Cartesian method, which is further demonstrated below with our numerical test (1) in Section 3.1.

Following Gerya and Yuen (2007) we applied a free-slip mechanical boundary condition for the model box (Fig. 1a) and used a high viscosity contrast between the weak massless medium and the outermost silicate layer instead of any boundary condition to control the surface of the body. This "weak medium approach" allows for the spontaneous formation of a free surface-like condition along the deforming planetary surface without prescribing this condition inside the model. Shear stresses along the surface are minimized by the low shear resistance of the weak medium. On the other hand, topography and normal stresses below the surface are properly captured by using the appropriate density contrast between the protoplanet and the weak massless-like medium. The validity of the weak layer approach has recently been tested and proven (Schmeling et al., 2008) with the use of a large variety of numerical techniques (including our I2ELVIS code) and comparison with analog modeling. The viscosity contrast needed between the protoplanet and the massless medium in order to obtain convergence of the numerical solution is shown below by our numerical test (5) in Section 3.1.

3. Results

3.1. Numerical accuracy tests

In this section we show results from several simplified accuracy tests which we performed to validate the code. These tests include the effects of

(1) Various initial perturbation directions.
(2) Amplitude of initial perturbation.
(3) Resolution of grid and marker.
(4) Position of gravity potential boundary.
(5) Viscosity contrast between the weak medium and the outer layer of the protoplanet.

The initial set up of benchmark tests for cases (1)–(5) is shown in Fig. 1a. The model box is 14,000 km × 14,000 km. Constant viscosity ($\eta = 10^{22}$ Pa s) is used for both silicate ($\rho = 4000$ kg m^{-3}, $d = 1000$ km) and metal ($\rho = 10,060$ kg m^{-3}, $d = 1000$ km) layers where d is the thickness of the corresponding layer. The protocore ($\rho = 5515$ kg m^{-3}, $R = 4000$ km) is 1000 times more viscous ($\eta = 10^{25}$ Pa s). The viscosity of the weak medium ($\rho = 1$ kg m^{-3}) is 1000 times lower ($\eta = 10^{19}$ Pa s) than the viscosity of the silicate

layer. The grid resolution of the model is 141 × 141 nodes (equal to a grid resolution of 100 × 100 km), with 10 × 10 markers per cell. The time-dependent evolution for the displacement of the protocore along the perturbation direction is shown in Fig. 2a.

We initiated the instability by perturbing the protocore from the center of the planetary body to a small distance of less than the width of a grid cell. This perturbation corresponds to the $L = 1$ mode of Rayleigh–Taylor instability as the fastest growing mode at the initial stage according to linear stability analysis (Ida et al., 1987). Fig. 2b shows that we have uniform results between different initial perturbation directions. Our model thus shows no sensitivity of the instability growth rate to the instability growth direction inside the Cartesian grid. This result proves the robustness of the applied spherical-Cartesian approach to model a self-gravitating body on a Cartesian grid (Gerya and Yuen, 2007).

We investigated the effect of the amplitude of initial perturbation ($x_0 = 0.14$, 1.4, 14 and 70 km). Logarithmic displacement is plotted as a function of time. The parallel curves in Fig. 2c during the linear instability stage (before the protocore hits the planetary surface and starts to deform) show that the different amplitudes still have the same growth rate σ ($\ln(x) = \sigma t + \ln(x_0)$) which represents the same evolution characteristic for the instability. The mode of deformation is thus insensitive to the magnitude of the initial perturbation.

A series of tests with an increase in grid resolution from 141 × 141 to 301 × 301 nodal points and with 4–400 markers per cell are shown in Fig. 2d and e. They demonstrate the convergence of numerical results with increasing numerical resolution (to 261 × 261–301 × 301 nodal points and to 5 × 5–10 × 10 markers per cell).

The gravity field is computed by solving the scaled Poisson equation in 2D (Eq. (3)) for the gravitational potential. The constant gravitational potential boundary condition (cf. Eqs. (10), (11)), is applied at a circular surface located at a certain distance from the protoplanet (cf. dashed line in Fig. 1a). Obviously this approach does not allow the reproduction of the spherical gravity field outside the protoplanet (Fig. 1b) but this area is of less significance for our study since we concentrate on deformation processes in the interior of the body. More importantly, forcing the potential to be uniform outside the protoplanet at a certain radius from the center of the body should also affect the gravitational field (especially its tangential component) and consequently deformation inside the protoplanet. To test significance of this latter effect for the case of large displacement of the primordial core caused by degree $L = 1$ instability we performed a series of experiments where the dynamics of the primordial core displacement was tested as a function of the position of the constant gravity potential boundary. Fig. 2f shows convergence of the solution with a moderate increase of this distance to 1/6–1 of the body radius. The convergence of the solution suggests that this method can be applied as a first approximation but more work is needed to elaborate and test better boundary conditions for the gravity. We therefore adopted a 1/2 body radius distance from the protoplanetary surface as our standard gravitational potential boundary position.

Fig. 2g reveals the effect of the viscosity of the weak massless medium surrounding the protoplanet. When the viscosity contrast at the body's interface increases to ⩾100–1000, the influence of the weak massless medium on the dynamics of instability growth becomes negligible and the protoplanetary surface behaves as a free surface. Therefore, we applied a high viscosity contrast of 1000 at the planetary surface in the following numerical tests and observed the changing shape of the protoplanet in the early stages of the internal reshaping process under this free surface condition, which is more realistic than the rigid boundary condition used by Honda et al. (1993).
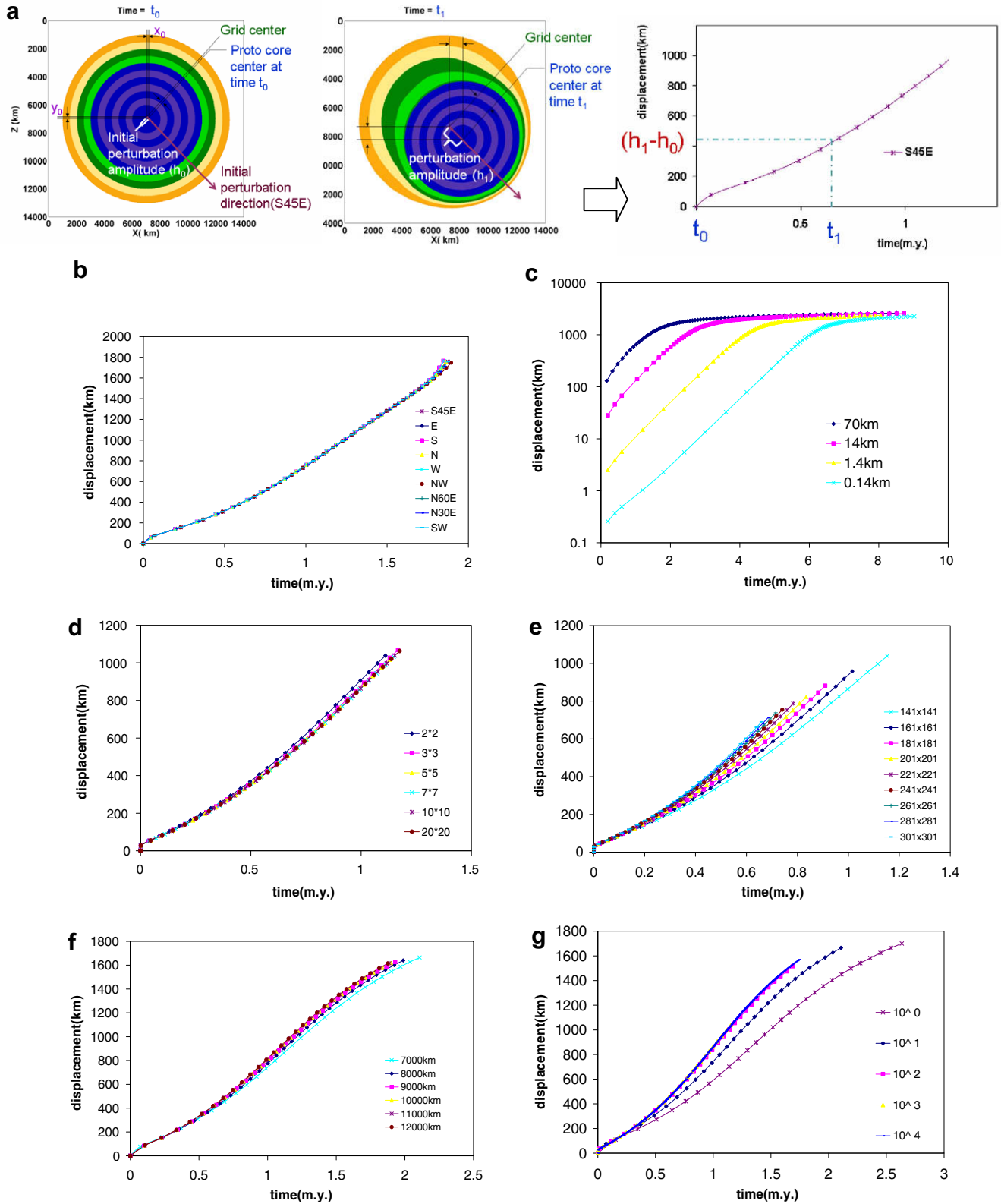
Fig. 2. Results of numerical accuracy tests. (a) Displacement of the protocore is measured as the distance between the grid center and the protocore center minus the initial perturbation amplitude. Numerical results for different cases testing the influences of variation in the (b) direction of initial perturbation; (c) amplitude of initial perturbation; (d) marker density; (e) numerical grid resolution; (f) position of gravitational potential boundary; (g) viscosity contrast between the weak medium and the outer silicate layer.

3.2. Benchmark with 3D analytic solutions

Finally we benchmarked our model against 3D analytic solutions by Ida et al. (1987). The primary goal of this benchmark is to check if relative changes in the L = 1 instability growth rate with changing 3D model parameters can be properly captured with our simplified 2D approach exploring a scaled cylindrical gravity field (Eq. (3)) and deformation. Fig. 3a shows the set up of these tests,

consisting of a two-layer model. The model box is 39,000 km × 39,000 km. The protoplanet (radius R_2 = 12,000 km) is composed only of a metal layer (ρ_2 = 9000 kg m^{-3}, thickness ΔR = 4000 km) and a protocore (ρ_1 = 4500 kg m^{-3}, R_1 = 8000 km). The radius of the protoplanet and the viscosities of the metal layer (η_2) and the protocore (η_1) are varied to create suitable conditions for comparison with results of Ida et al. (1987). We applied a thin strong massless layer (d = 1000 km, viscosity is 1000 times higher than the one employed for the metal layer) around the protoplanet to enforce a rigid boundary, as is used in the analytic solutions. The rest of the region is occupied by a weak massless medium with 1000 times lower viscosity than the strong massless layer. The grid resolution of the model is 261 × 261 nodes (150 km × 150 km), with 6,760,000 markers.

The growth rate σ is plotted in Fig. 3b as a function of S_2, which is a non-dimensional parameter indicating the degree of efficiency of viscosity (Ida et al., 1987)

$$S_2 = \eta_2/\rho_2 R_1 \Delta R \sigma_f \tag{12}$$

$$\sigma_f = \sqrt{4\pi\gamma(\rho_2 - \rho_1)/3} \tag{13}$$

where σ_f is the free-fall growth rate.

As follows from Fig. 3b, relative changes in growth rate computed numerically in 2D with our scaled cylindrical approach (Eq. (3)) are quite consistent with the 3D analytical solution over a broad range of model parameters corresponding to a non-inertial internal reshaping mode characterized by higher viscosity of the metal layer and respectively larger values of S_2. In this viscous reshaping regime the two solutions are parallel, and analytical and numerical growth rates differ by a factor of around 2, which can be used for a systematic correction of 2D numerical results. Finally, we would like to point out that in the present paper we explore a greatly simplified three-layer structure of the planet and a Newtonian rheological model. Therefore we are not aiming to evaluate precisely the exact duration of reshaping processes in protoplanetary bodies but rather evaluate qualitatively changes in this duration caused by variations in model parameters.

## 3.3. Viscosity structure experiments

3.3.1. Experiment setup

Here we report viscosity structure experiments for a three-layer model. We take the Mars-sized case with 3400 km body radius as a reference example (tests62–70 in Table 1). The model box is 10,200 km × 10,200 km and the grid resolution is 151 × 151 nodes,

with 562,500 markers. The numerical grid resolution used is moderate (cf. Fig. 2e) since we aimed to systematically compare the geometry and relative dynamics of internal reshaping but not to evaluate precisely the rate of this process. We used the parameters of the protocore (R_1 = 2165 km, ρ_1 = 6000 kg m^{-3}) with the ratios (R_2/R_1 = 1.28, R_3/R_1 = 1.57, ρ_2/ρ_1 = 1.67, ρ_3/ρ_1 = 0.83) adopted from Honda et al. (1993) to derive parameters of the silicate layer (ρ_3 = 4980 kg m^{-3}, d_3 = 628 km) and metal layer (ρ_2 = 10,020 kg m^{-3}, d_2 = 607 km), where subscripts 1, 2, 3, 4 stand for the protocore, metal layer, the silicate layer, and the massless medium. The instability of the metal layer may occur before the iron thickness we adopted has been reached. The initiation time is a function of the protocore viscosity. The effect of the iron thickness is on the size and the growth rate of the formation of the first iron drop. The thicker the iron layer, the larger the iron drop and a shorter time required for the formation of the iron core (Honda et al., 1993).

The viscosities of the three layers are varied by using two ratios, η_2/η_3 and η_1/η_3, whereas the metal viscosity ($\eta_2 = 10^{18}$ Pa s) was fixed for all the experiments as the growth rate of core formation would be influenced by the viscosity of the metal layer (Ida et al., 1987). The iron viscosity has been suggested to be 10^{-2} Pa s (Rubie et al., 2007), orders of magnitude lower, however it is not possible with today's numerical techniques to perform numerical models with such a huge viscosity contrast. Therefore, the later discussion is based on the relative viscosity contrast between the three layers. The weak massless medium filling the empty region has a viscosity 1000 times lower than the outermost silicate layer (η_3/η_4 = 1000) for simulations tests1–56 and tests62–79, where tests50–56 reproduced the results by Honda et al. (1993). We explored the effects of a fixed boundary on the planet's surface by applying the massless medium as the strongest material of the whole model with a viscosity 1000 times higher than the strongest materials of the planet ($\eta_4/\eta_{strongest}$ = 1000) for selected viscosity ratios in tests57–61.

In our experiments we also changed the radius of the protoplanet to 5000 km (Earth-sized body, tests1–49) and to 2500 km (Mercury-sized body, tests71–79) keeping all ratios between thicknesses and density of different layers constant.

Table 1 summarizes the parameter values used in the numerical tests and Fig. 4 shows the relative location of tests1–79 in a viscosity-ratio coordinate system, where the metal/silicate (η_2/η_3) and the protocore/silicate (η_1/η_3) viscosity ratio are plotted. The results of nine experiments for Mars-sized bodies are shown each in three figures to demonstrate the planetary evolution with time during the metallic core formation. The selected experiments are marked
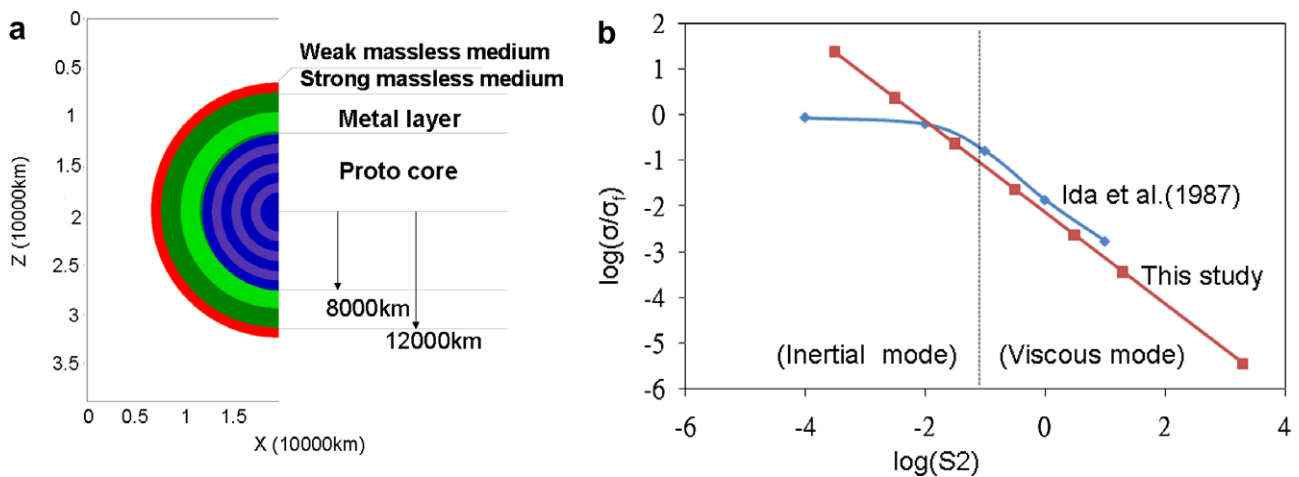
Fig. 3. Numerical setup (a) and comparison (b) between numerical (this study) and analytical (Ida et al., 1987) solutions.

Table 1
Parameters of conducted numerical experiments.

Test	Case	$\eta2/\eta3$	$\eta1/\eta3$	$\eta4$	$\eta3$	$\eta2$	$\eta1$
Tests for Earth-sized bodies (R_1 = 3200 km, R_2 = 4096 km, R_3 = 5024 km)							
1	I	1000	0.001	10^{12}	10^{15}	10^{18}	10^{12}
2		1000	0.01	10^{12}	10^{15}	10^{18}	10^{13}
3		1000	0.1	10^{12}	10^{15}	10^{18}	10^{14}
4	F	1000	1	10^{12}	10^{15}	10^{18}	10^{15}
5		1000	10	10^{12}	10^{15}	10^{18}	10^{16}
6		1000	100	10^{12}	10^{15}	10^{18}	10^{17}
7	C	1000	1000	10^{12}	10^{15}	10^{18}	10^{18}
8		100	0.001	10^{13}	10^{16}	10^{18}	10^{13}
9		100	0.01	10^{13}	10^{16}	10^{18}	10^{14}
10		100	0.1	10^{13}	10^{16}	10^{18}	10^{15}
11		100	1	10^{13}	10^{16}	10^{18}	10^{16}
12		100	10	10^{13}	10^{16}	10^{18}	10^{17}
13		100	100	10^{13}	10^{16}	10^{18}	10^{18}
14		100	1000	10^{13}	10^{16}	10^{18}	10^{19}
15		10	0.001	10^{14}	10^{17}	10^{18}	10^{14}
16		10	0.01	10^{14}	10^{17}	10^{18}	10^{15}
17		10	0.1	10^{14}	10^{17}	10^{18}	10^{16}
18		10	1	10^{14}	10^{17}	10^{18}	10^{17}
19		10	10	10^{14}	10^{17}	10^{18}	10^{18}
20		10	100	10^{14}	10^{17}	10^{18}	10^{19}
21		10	1000	10^{14}	10^{17}	10^{18}	10^{20}
22	H	1	0.001	10^{15}	10^{18}	10^{18}	10^{15}
23		1	0.01	10^{15}	10^{18}	10^{18}	10^{16}
24		1	0.1	10^{15}	10^{18}	10^{18}	10^{17}
25	E	1	1	10^{15}	10^{18}	10^{18}	10^{18}
26		1	10	10^{15}	10^{18}	10^{18}	10^{19}
27		1	100	10^{15}	10^{18}	10^{18}	10^{20}
28	B	1	1000	10^{15}	10^{18}	10^{18}	10^{21}
29		0.1	0.001	10^{16}	10^{19}	10^{18}	10^{16}
30		0.1	0.01	10^{16}	10^{19}	10^{18}	10^{17}
31		0.1	0.1	10^{16}	10^{19}	10^{18}	10^{18}
32		0.1	1	10^{16}	10^{19}	10^{18}	10^{19}
33		0.1	10	10^{16}	10^{19}	10^{18}	10^{20}
34		0.1	100	10^{16}	10^{19}	10^{18}	10^{21}
35		0.1	1000	10^{16}	10^{19}	10^{18}	10^{22}
36		0.01	0.001	10^{17}	10^{20}	10^{18}	10^{17}
37		0.01	0.01	10^{17}	10^{20}	10^{18}	10^{18}
38		0.01	0.1	10^{17}	10^{20}	10^{18}	10^{19}
39		0.01	1	10^{17}	10^{20}	10^{18}	10^{20}
40		0.01	10	10^{17}	10^{20}	10^{18}	10^{21}
41		0.01	100	10^{17}	10^{20}	10^{18}	10^{22}
42		0.01	1000	10^{17}	10^{20}	10^{18}	10^{23}
43	G	0.001	0.001	10^{18}	10^{21}	10^{18}	10^{18}
44		0.001	0.01	10^{18}	10^{21}	10^{18}	10^{19}
45		0.001	0.1	10^{18}	10^{21}	10^{18}	10^{20}
46	D	0.001	1	10^{18}	10^{21}	10^{18}	10^{21}
47		0.001	10	10^{18}	10^{21}	10^{18}	10^{22}
48		0.001	100	10^{18}	10^{21}	10^{18}	10^{23}
49	A	0.001	1000	10^{18}	10^{21}	10^{18}	10^{24}
Experiments of Honda et al. (1993)							
50		0.03	1	3.33×10^{18}	3.33×10^{21}	10^{20}	3.33×10^{21}
51		0.03	1	3.33×10^{18}	3.33×10^{21}	10^{20}	3.33×10^{21}
52		0.03	1	3.33×10^{18}	3.33×10^{21}	10^{20}	3.33×10^{21}
53		0.03	1	3.33×10^{18}	3.33×10^{21}	10^{20}	3.33×10^{21}
54		0.03	1	3.33×10^{18}	3.33×10^{21}	10^{20}	3.33×10^{21}
55		0.03	1	3.33×10^{18}	3.33×10^{21}	10^{20}	3.33×10^{21}
56		0.03	1	3.33×10^{18}	3.33×10^{21}	10^{20}	3.33×10^{21}
Tests for Earth-sized bodies with fixed boundary							
57	I	1000	0.001	10^{21}	10^{15}	10^{18}	10^{12}
58	C	1000	1000	10^{21}	10^{15}	10^{18}	10^{18}
59	G	0.001	0.001	10^{24}	10^{21}	10^{18}	10^{18}
60	A	0.001	1000	10^{27}	10^{21}	10^{18}	10^{24}
61	E	1	1	10^{21}	10^{18}	10^{18}	10^{18}
Tests for Mars-sized bodies (R_1 = 2165 km, R_2 = 2772 km, R_3 = 3400 km)							
62	I	1000	0.001	10^{12}	10^{15}	10^{18}	10^{12}
63	F	1000	1	10^{12}	10^{15}	10^{18}	10^{15}
64	C	1000	1000	10^{12}	10^{15}	10^{18}	10^{18}
65	H	1	0.001	10^{15}	10^{18}	10^{18}	10^{15}
66	E	1	1	10^{15}	10^{18}	10^{18}	10^{18}
67	B	1	1000	10^{15}	10^{18}	10^{18}	10^{21}
68	G	0.001	0.001	10^{18}	10^{21}	10^{18}	10^{18}
69	D	0.001	1	10^{18}	10^{21}	10^{18}	10^{21}
70	A	0.001	1000	10^{18}	10^{21}	10^{18}	10^{24}

Table 1 (continued)

Test	Case	η_2/η_3	η_1/η_3	η_4	η_3	η_2	η_1
Tests for Mercury-sized bodies (R_1 = 1600 km, R_2 = 2048 km, R_3 = 2512 km)							
71	I	1000	0.001	10^{12}	10^{15}	10^{18}	10^{12}
72	F	1000	1	10^{12}	10^{15}	10^{18}	10^{15}
73	C	1000	1000	10^{12}	10^{15}	10^{18}	10^{18}
74	H	1	0.001	10^{15}	10^{18}	10^{18}	10^{15}
75	E	1	1	10^{15}	10^{18}	10^{18}	10^{18}
76	B	1	1000	10^{15}	10^{18}	10^{18}	10^{21}
77	G	0.001	0.001	10^{18}	10^{21}	10^{18}	10^{18}
78	D	0.001	1	10^{18}	10^{21}	10^{18}	10^{21}
79	A	0.001	1000	10^{18}	10^{21}	10^{18}	10^{24}

with blue squares and organized into three groups I, II, and III (Fig. 4), which are presented in Figs. 5–7.

3.3.2. Reference case

Case A (test70 in Table 1, see Fig. 5) illustrates the reference mode of core formation observed in our experiments, where protocore is the strongest material and metal is the weakest one while silicate has an intermediate viscosity between the two. It can be roughly divided into three phases. First, the protocore is promoted by the degree-one Rayleigh–Taylor instability to move away from the protoplanet's center to the surface. Second, the body starts to deform as the protocore hits the protoplanetary surface due to the accumulation of metal material at the antipode. During the third stage the metal enters the protoplanet's center to form the metal core while the protocore material and the disturbed outermost silicate layer redistributes around the newly formed core. As final stage we observe the accumulation of secondary metal drops following the formation of the central metal core. However, the development of secondary metal drops in this reference case is very slow because of the small thickness of the remaining metallic layer and the high viscosity of the protocore. The key feature of this case is that the relative high viscosity of the protocore keeps its shape spherical until it hits the body's surface and even changes the whole protoplanet to an aspherical shape. Following that, the protocore is exposed to the surface and pushes the magma ocean (silicate layer) apart. The moment when the protocore reaches the closest distance to the protoplanetary surface is marked for all simulations with a red square around it (see Figs. 5–7). This represents the maximum degree of exposure of the protocore and is used for further analysis. The behavior of the aspherical deviation of the protoplanet's shape and exposure of the protocore may become more moderate if we account for thermal effects in the calculation. This can be shown through the variation of the viscosity contrasts between protocore and the other two layers if we assume the viscosity contrasts are controlled by the temperature in the following tests.

3.3.3. Influence of metal viscosity

The influence of metal viscosity can be seen by comparison of the simulations in the group I (see Fig. 5). The viscosity of metal layer increases relatively through cases A–C. Comparing the first picture of each test, the protocore deforms more easily with increasing viscosity of the metal and in models cases B and C the deformation happens already on the way to the surface, while the reference case (case A) keeps its shape until hitting the protoplanetary surface. However group II (see Fig. 6), where the viscosity of metal also increases from the left to the right column, shows that strong metal can push the protocore away from the protoplanet's center. Due to this less silicate and metal material is to be left behind (see second row in Fig. 6). Group III in Fig. 7 shows the same effect, less leftover silicate and metal material in results cases H and I. The viscosity combination of three layers may not be realistic in any planetary body in cases I and F as the iron layer is the strongest material. However, these tests help us to clarify the influence of the iron layer on the core destabilization mechanism.

3.3.4. Influence of silicate and protocore viscosity

We compared the results of cases A, D and G, which are presented as the first column pictures in Figs. 5–7, to see the effect of the silicate viscosity on the process. As the viscosity of the silicate layer increases relatively through case A–D and G, the deformation concentrates in the interior of the body. This helps to keep the spherical shape of the protoplanet. Combined with the effect of decreasing viscosity of the protocore, it is much easier to form secondary metal drops, and the pattern of case G is similar to the prediction of Elsasser (1963), that is, the creation of a metal core by accumulation of a big iron drop over time.

3.3.5. The influence of the size of the body

Fig. 8 shows one snapshot for each of nine selected experiments with Mercury-size and Fig. 9 with Earth-sized protoplanets during the first stage of core formation. As follows from comparison of Figs. 8 and 9 with respective stages of development obtained for Mars-sized models (cf. first stages for respective cases in Figs. 5–7). The identified geometrical modes of planetary reshaping do not depend on the planetary size which is due to assumed sim-
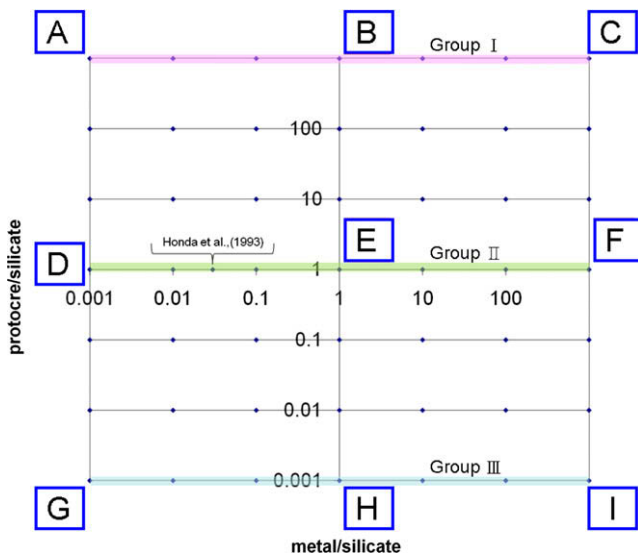
Fig. 4. Conditions of conducted numerical experiments (dots) shown in metal/silicate (η_2/η_3) and protocore/silicate (η_1/η_3) coordinates. Runs marked with blue squares are shown in Figs. 5–7. (For interpretation of the references to color in this figure legend, the reader is referred to the web version of this article.)
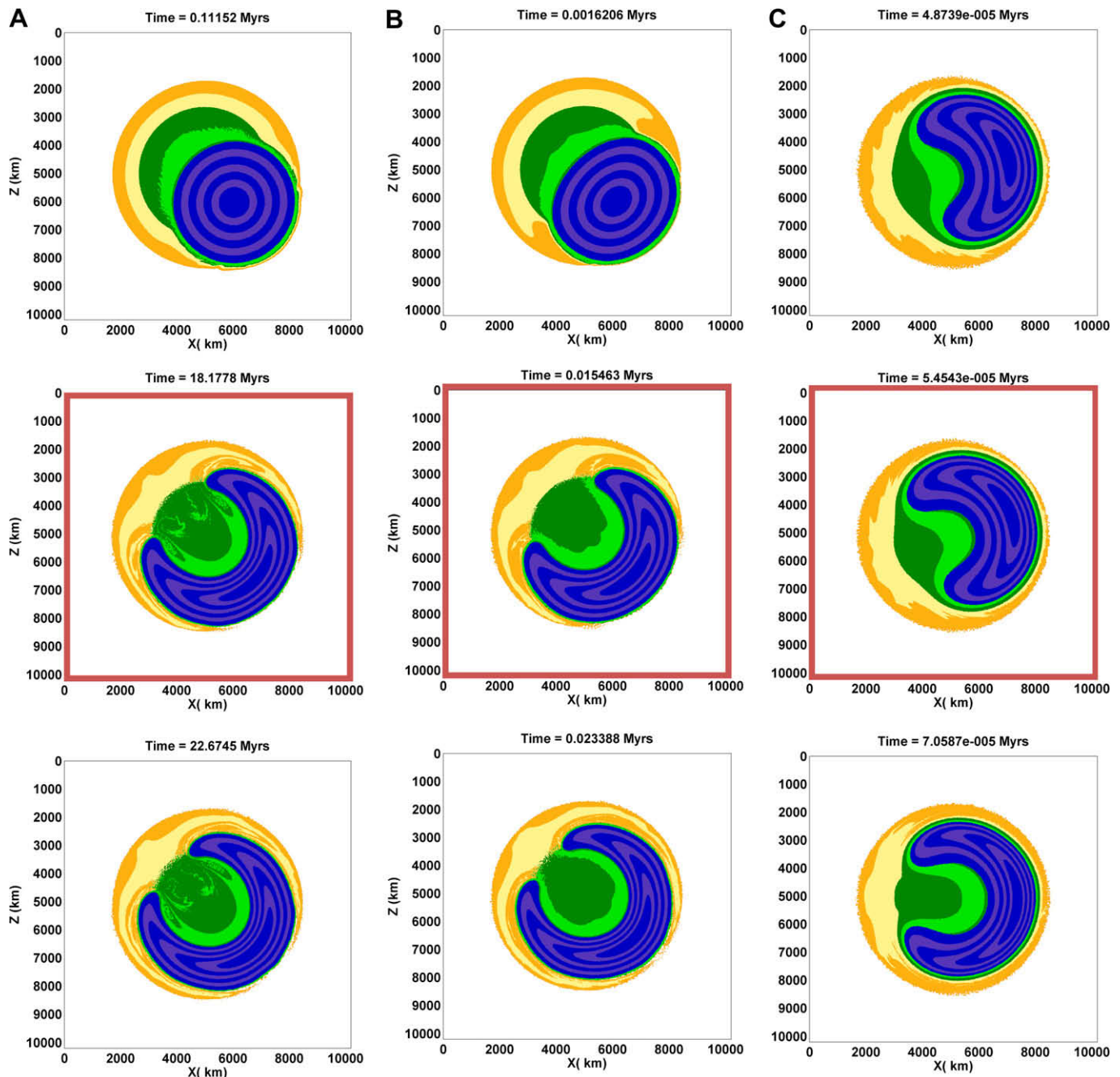
Fig. 5. Numerical results for group I from Fig. 4 for Mars-sized bodies (A = test70, B = test67 and C = test64 in Table 1). Three selected figures from each test represent time evolution shown in one column. Figures marked with red squares are the snapshots for the moment of the maximal exposure of the protocore (i.e. shortest distance between the protocore and the surface) in each test. (For interpretation of the references to color in this figure legend, the reader is referred to the web version of this article.)

plified viscosity and density structure of our models. Therefore, in the following we discuss the reshaping process mainly based on the results of our most systematic Earth-sized experiments (tests1–69 in Table 1).

3.3.6. Influence of a fixed surface

Fig. 10 demonstrates the effect of a fixed boundary around an Earth-sized body for 3 cases, A, C, and G. These three cases represent the extreme cases of viscosity structure (see Table 1). The results show that the reshaping process acts with notable similarities to some of the previous cases that have a strong silicate layer: The deformation inside the protoplanet in cases A and C is more limited and the protocore exposure is less pronounced, while case

G has no significant change since it has a strong silicate layer originally. Thus, the boundary condition will notably affect the reshaping of the protoplanet during the early stage of the core formation, if the silicate viscosity is low compared to either protocore or metal.

4. Discussion

4.1. Aspherical deviation of the protoplanet

First, we measured the maximum distance of aspherical deviation of the Earth-sized protoplanet (Fig. 11a) and obtained the stretching distance after subtracting the diameter of the body as
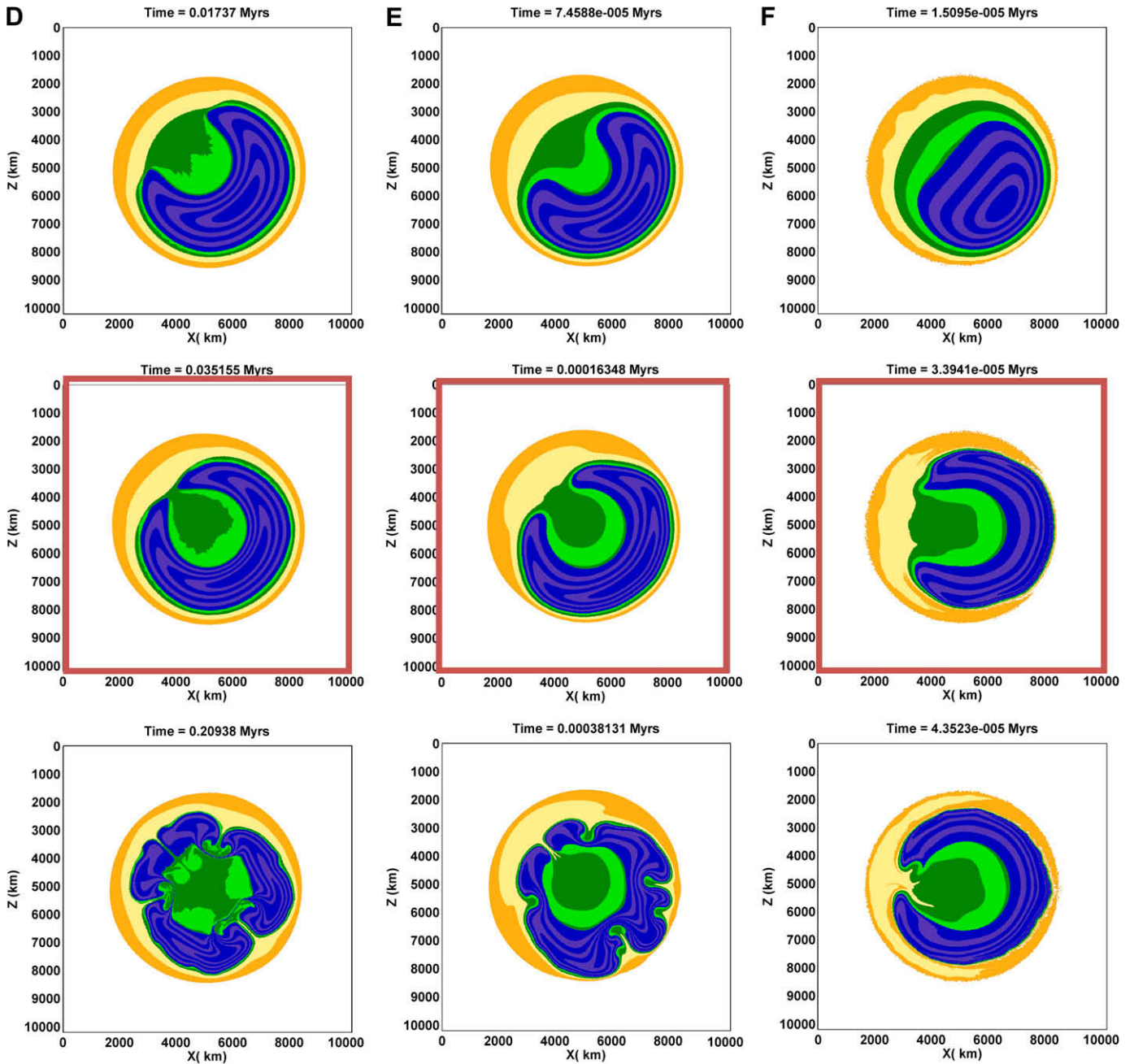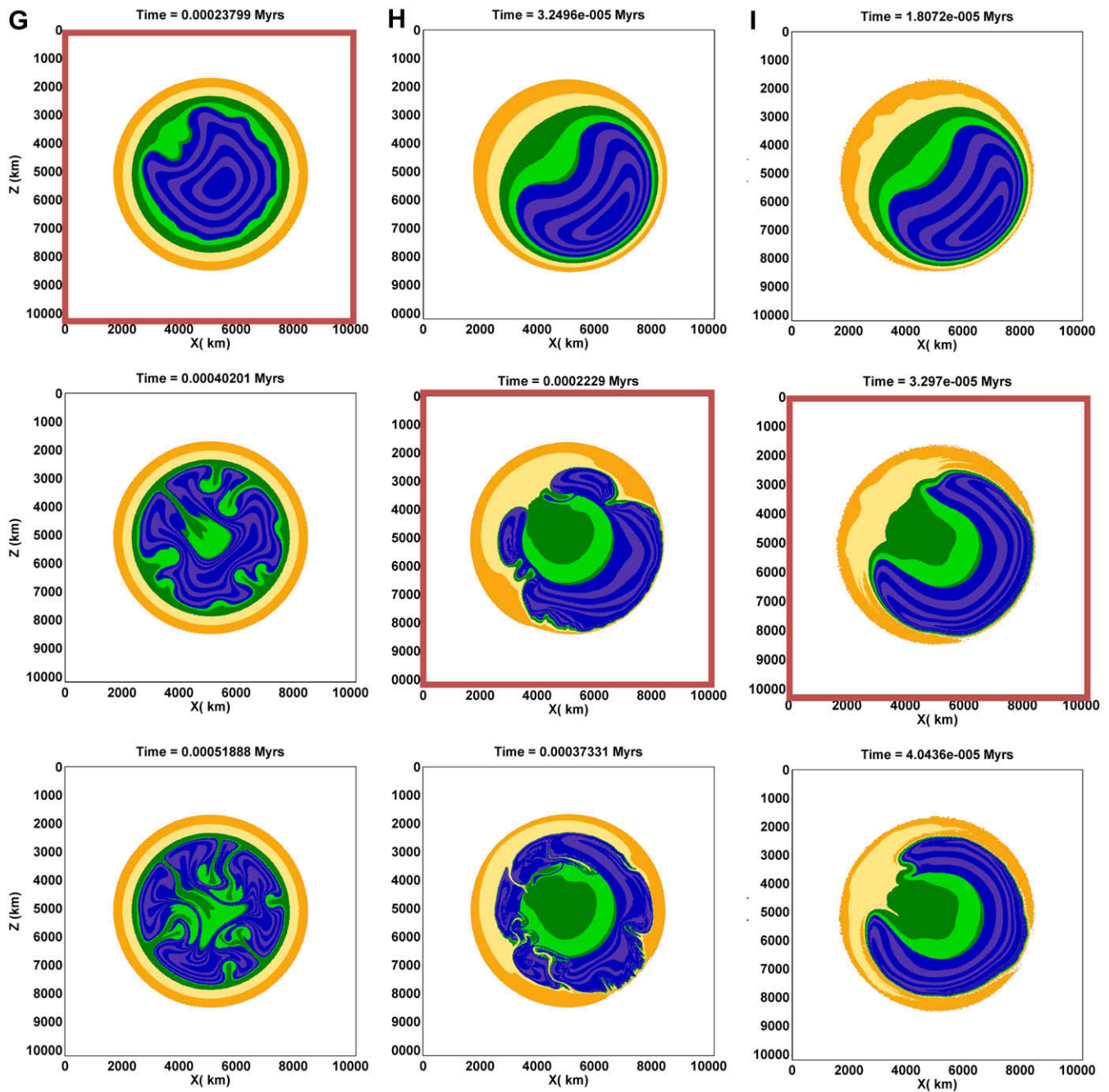
Fig. 6. Numerical results for group II from Fig. 4 for Mars-sized bodies (D = test69, E = test66 and F = test63 in Table 1). Three selected figures from each test represent time evolution shown in one column. Figures marked with red squares are the snapshots for the moment of the maximal exposure of the protocore in each test. (For interpretation of the references to color in this figure legend, the reader is referred to the web version of this article.)

shown in Fig. 11b in viscosity-ratio coordinate, which indicates the degree of aspherical deviation of the planet. The maximum deviation (up to 500 km, which is around 8% of the diameter) happens in the upper-left corner of Fig. 11b, which we take as the most realistic cases for a cold interior assumption (Sasaki and Nakazawa, 1986; Karato and Murthy, 1997; Senshu et al., 2002) in which the solid protocore is the strongest material, and molten silicate is stronger than molten metal. The viscosity estimate for the protocore ranges from 10^{18} to 10^{28} Pa s (Karato and Murthy, 1997), and for molten iron it is from 10^{-2} to 10^{-3} Pa s (Rubie et al., 2007). Molten silicates are roughly one order of magnitude more viscous than molten iron when the temperature is within the range from 1500 K to 3000 K (Rubie et al., 2003). Weak protocores always result in a small aspherical deviation of the protoplanet. If we consider the

thermal feedback such as shear heating or gravitational heat release during iron migration to the core, it might reduce the deviation because of the temperature dependence of the viscosity. Obviously the aspherical deviation of the planetary body was not observed by Honda et al. (1993) since a rigid planetary boundary was used in their numerical experiments.

The degree of protocore exposure is evaluated by measuring the minimum distance of the protocore to the surface as shown in Fig. 11c and the results of the measurement are shown in Fig. 11d. In Fig. 11d we observe that the strongest exposure happens when the relative viscosity of either protocore or metal is the highest in the model. The viscosity of the silicate layer is the dominant factor precluding the exposure of the protocore (cf. the diagonal trend of minimal protocore exposure in Fig. 11d). The higher the viscosity

Fig. 7. Numerical results for group III from Fig. 4 for Mars-sized bodies (G = test68, H = test65 and I = test62 in Table 1). Three selected figures from each test represent time evolution shown in one column. Figures marked with red squares are the snapshots for the moment of the maximal exposure of the protocore in each test. (For interpretation of the references to color in this figure legend, the reader is referred to the web version of this article.)

of the silicate layer, the less exposure of the protocore is observed as the deformation in this case is concentrated on the interior of the protoplanet and as the result a smaller first iron drop is formed. It is also worth mentioning that the protocore exposure was not identified in the numerical experiments of Honda et al. (1993) since the viscosity of the silicate in these experiments was relatively high and the conditions of their experiments (Fig. 11d) were close to the diagonal trend of minimum protocore exposure.

The exposure of the protocore can cause strong lateral variation in the depths of the magma ocean around the protoplanet and may have notable geochemical consequences caused by variations in pressure at the bottom of the magma ocean, which would affect for example FeO partitioning into liquid iron (Asahara et al., 2007). When some part of these cold accreted protoplanets is about to be accreted by the forming terrestrial planets (e.g. Chambers and Wetherill, 2001) these bodies could have a significantly different geochemical signature. The question of whether equilibration of the impactor's material on the growing terrestrial planets via emulsification of impactor cores as proposed by Rubie et al. (2003) is possible is still under debate (e.g. Stevenson, 2008). This could have a significant influence on the geochemical signature of the final terrestrial planets.
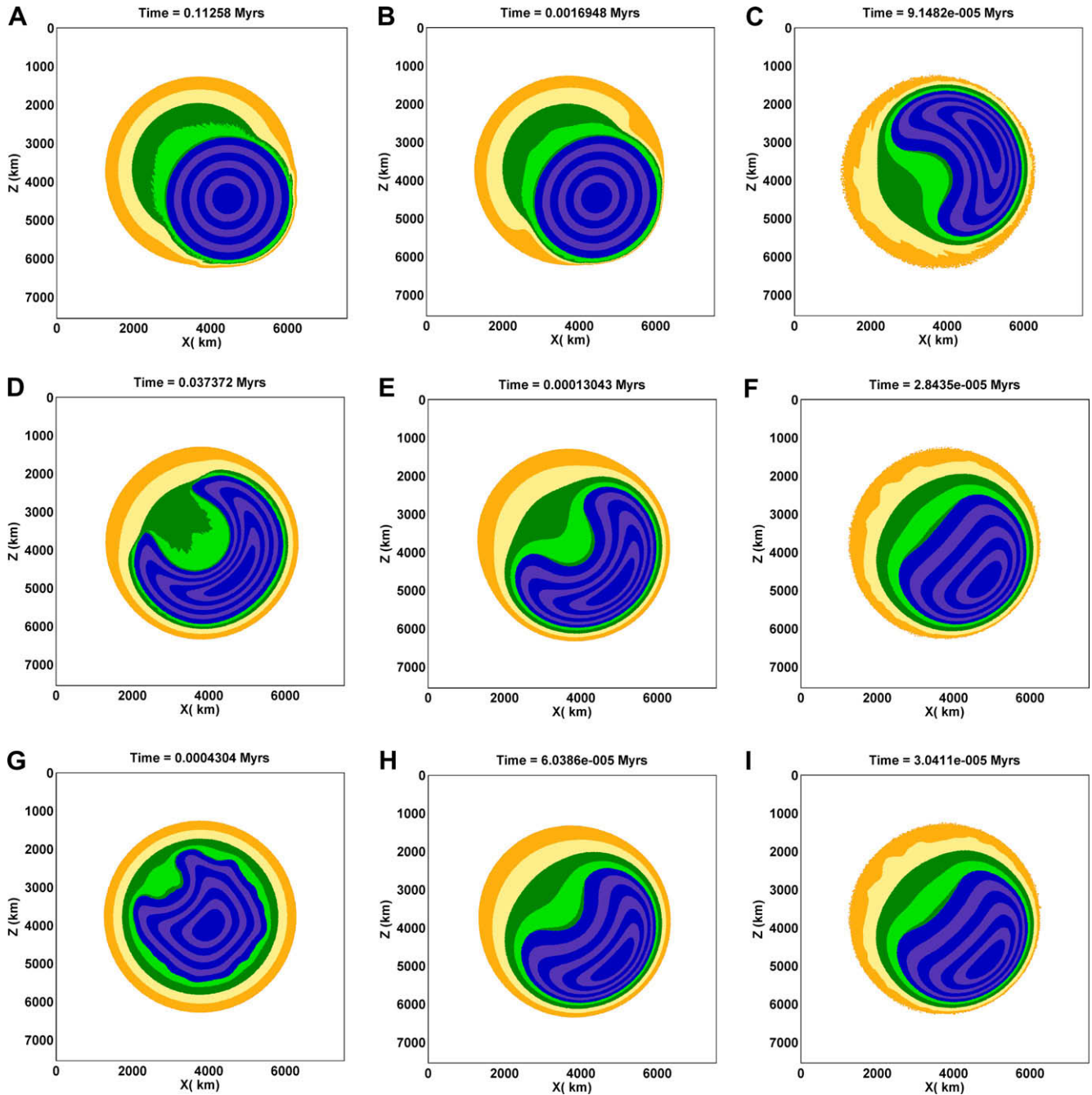
Fig. 8. Numerical results for nine experiments for Mercury-sized bodies (A = test79, B = test76, C = test73, D = test78, E = test75, F = test72, G = test77, H = test74 and I = test71 in Table 1). Each experiment is presented by one snapshot during the first stage of core formation.

4.2. Timescale of metallic core formation

In most of our experiments (Figs. 5–7) the timescale of metallic core formation is defined mainly by the viscosity of the protocore. We evaluated the time scale of protocore deformation by picking two arbitrary but geometrically well defined snapshots: (1) the accumulated iron drop starts to push away the protocore and forms a straight line between them (Fig. 12a), and (2) the protocore starts to surround the newly formed iron core so that two parallel boundaries of the metallic core can be observed (Fig. 12b). These two stages can be observed in all conducted tests, which allow a uniform comparison of protocore deformation timescales. The time duration calculated as the time difference between two snapshots, is shown in Fig. 12c in viscosity-ratio coordinate. The duration time

in Fig. 12c follows the diagonal trend, which illustrates that the time is controlled by the viscosity product of protocore and metal. The higher the value of the product, the more time is needed to deform the protocore. For experiments with the protocore stronger than the metal (which is obviously the most realistic situation) the protocore deformation time is linearly dependent on the protocore viscosity (Fig. 12d). A notable deviation from the linearity starts when the protocore viscosity is low compared to silicate and metal. As shown in Fig. 12d the deviation in this case is controlled by the viscosity ratio between metal and silicate.

As mentioned above the geometry of the reshaping process is independent of the size of the protoplanet, however this size has a strong effect on the timescale of the core formation (Fig. 13). Compared to Earth-sized experiments (Fig. 12) the gravitational
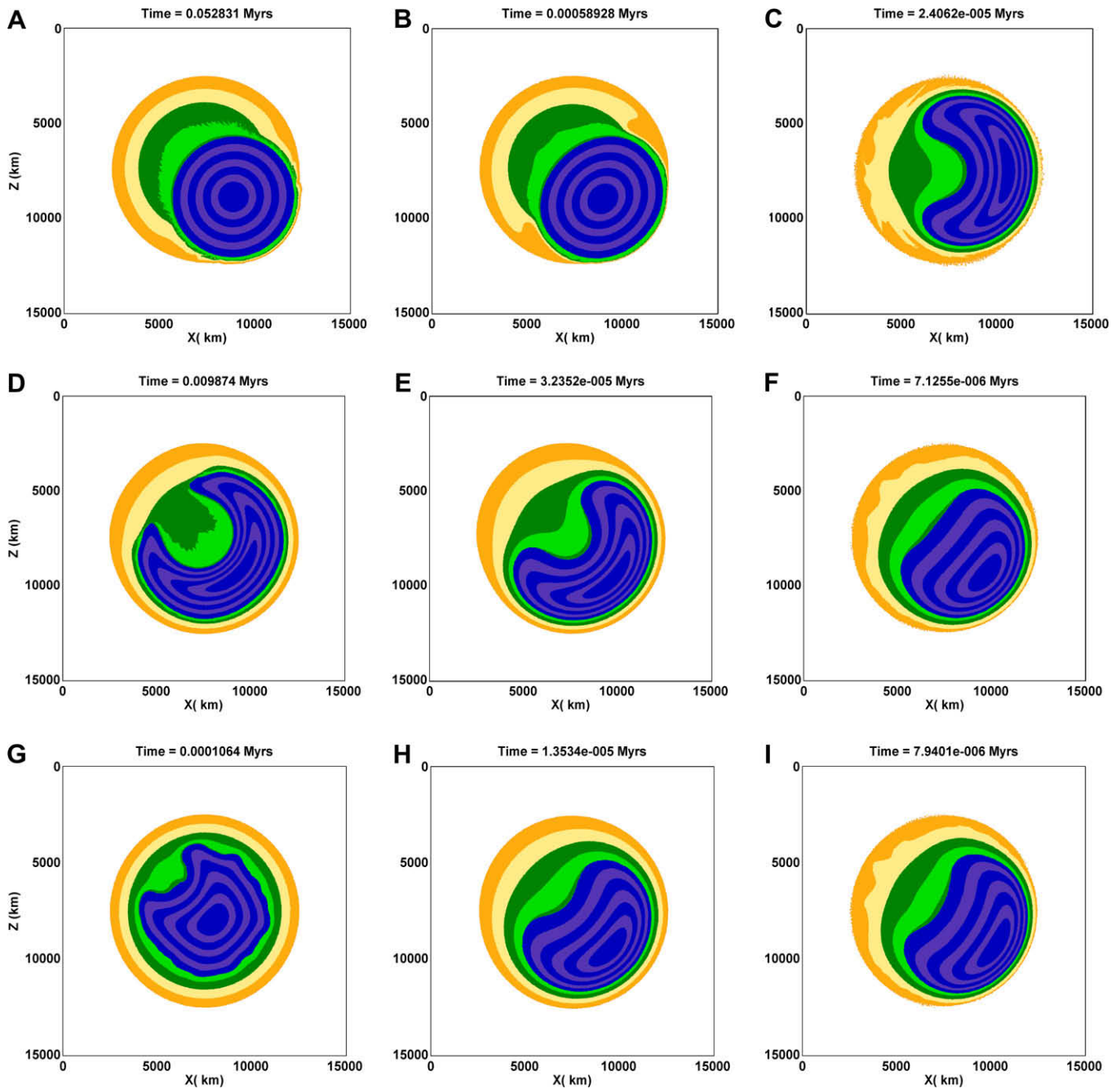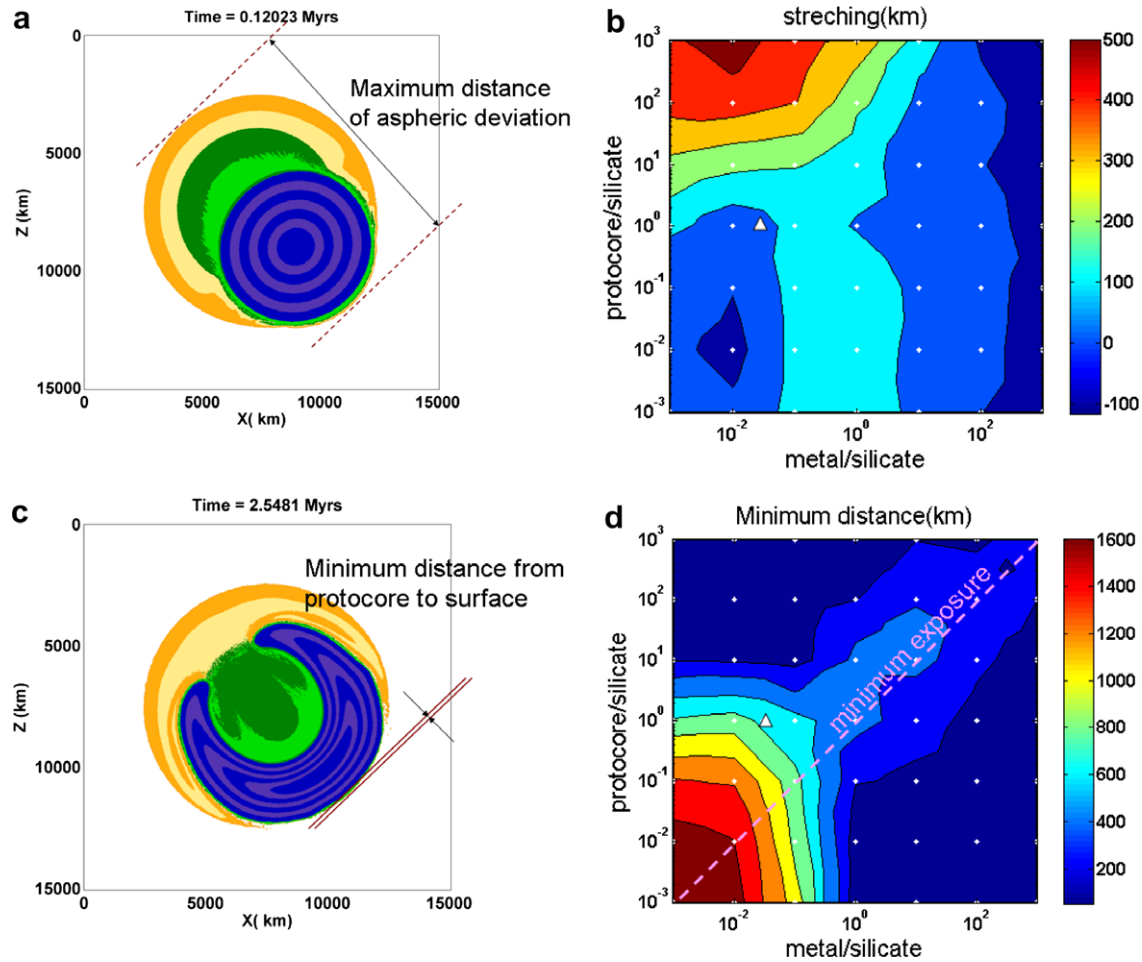
Fig. 9. Numerical results for nine selected experiments for Earth-sized bodies (A = test49, B = test28, C = test7, D = test46, E = test25, F = test4, G = test43, H = test22 and I = test1 in Table 1). Each experiment is presented by one snapshot during the first stage of core formation.

redistribution process inside smaller bodies is notably slower (two times and four times slower for Mars-sized and Mercury-sized bodies, respectively) due mainly to the reduction of the gravity in Eq. (5). Such relatively simple relationships are obviously pre-defined by the chosen highly simplified model setup assuming constant viscosity and density of all materials and thus not taking into account effects of temperature increase caused by gravitational energy dissipation. In nature such effects may strongly affect internal reshaping mode with changing size of the planetary body.

We estimated the metallic core formation time in our Earth-sized experiments as the moment when ~80% iron is accumulated in the center of the protoplanet (Fig. 12f). As seen from Fig. 12f in the case of a strong protocore, the timescale of metallic core formation is mainly defined by the protocore viscosity. The dependence is, however, non-linear, reflecting interplays between different

modes of reshaping and metallic core aggregation found in different numerical experiments (Figs. 5–7). Combined with the linear dependence on the protocore viscosity (Fig. 12d) and body size (Fig. 13) and taking into account possible uncertainty of our scaled 2D approach (Fig. 3b), we suggest that it takes several million to a few tens of million years to complete core formation on a Mercury-to Earth-sized body when the effective protocore viscosity is over 10^{24} Pa s, which is in good agreement with the results of ~10 Myr suggested by Honda et al. (1993) for Earth-sized bodies. Further studies should include more realistic rheology of the protocore, such as thermal feedback from shear heating (Senshu et al., 2002; Gerya and Yuen, 2007) and a change of the deformation mechanism in the high stress regime to pressure-, temperature- and stress-dependent dislocation creep and Peierls plasticity in order to have a better estimate of core formation time,

Fig. 10. Numerical results for case A, case C, and case G (Fig. 4) with free and fixed (rigid) surface boundary around an Earth-sized body. Three selected figures from each test represent time evolution shown in one column. Figures marked with red squares are the snapshots for the moment of the maximal exposure of the protocore in each test. (a) = Case A (tests49 and 60 in Table 1) (b) = case C (tests7 and 58 in Table 1) (c) case G (tests43 and 59 in Table 1). (For interpretation of the references to color in this figure legend, the reader is referred to the web version of this article.)

Fig. 11. Numerical results for aspherical deviation of planetary shape and protocore exposure computed for Earth-sized bodies (tests1–49 in Table 1). (a) Maximum distance of aspherical deviation of the protoplanet. (b) Stretching distance derived by subtracting the protoplanet's diameter from the maximum distance of aspherical deviation. (c) Minimum distance from the protocore to the protoplanetary surface. (d) Dependence of this distance from modeled metal/silicate and protocore/silicate viscosity ratios. The white triangle shows conditions for numerical experiments of Honda et al. (1993).

as the rheology of the protocore should change during core forma-
tion rather than keeping the same uniform viscosity as in our pres-
ent simplified simulation.

4.3. Modes of reshaping

As in the snapshot of Fig. 12b we also measured the size of the
first iron drop (forming the metallic core) and the result is in
Fig. 12e, which also shows the same trend as the maximum defor-
mation map in Fig. 11d. Higher strength of protocore/metal results
in a bigger size of the first iron drop. Hence the viscosity contrast
between the three layers could also be the key factor to influence
the modes of reshaping. The most realistic case is case A (Fig. 5),
corresponding to the degree $L = 1$ mode, and case G (Fig. 7) in the
left-lower corner of Fig. 4, which involves several big iron drops
(degree $L \geqslant 2$ mode) as suggested by Elsasser (1963). Hence during
core formation, as the viscosity contrast between the layers
decreases by the gravitational energy release, the instability might
change to higher order modes.

The first diapirs created from degree-one instability are at least
2/3 of the body radius (e.g. ~2000 km for Earth-sized body in
Fig. 12e). The subsequent iron drops may have much smaller size,
which cannot be resolved by this model; however the sum of
secondary drops is small in volume compared to the first one.

At the end of the simulation the remnants of the metallic layer
still create settling iron drops forming small scale heterogeneity in

the mantle and at the core-mantle boundary and displacing vari-
ous materials downward. Therefore, the end of the core formation
process will result in highly heterogeneous starting conditions for
global mantle convection.

4.4. Model limitations

The numerical models presented here have both methodologi-
cal and conceptual limitations. In particular our quasi spherical 2D
approach does not allow to model properly gravitational accelera-
tion outside the protoplanet which is notably overestimated
(Fig. 1b). A potential way out of this problem is to use 3D model-
ing with similar methodology based on a Cartesian grid as was
recently outlined by Gerya and Yuen (2007). Moreover, forcing
the potential to be uniform outside the protoplanet at a certain
radius from the center of the body should also affect the gravita-
tional field (especially its tangential component) and consequently
deformation inside the protoplanet. Therefore more work is
needed for moving the gravity potential boundary away from
the planetary domain (e.g. by using non-uniform grids) and imple-
menting a more sophisticated infinity-like boundary condition for
the gravity potential which will help eliminate this problem. Last
but not least, the rheological model used in this study is highly
oversimplified and strong thermomechanical feedbacks from grav-
itational energy dissipation (e.g. Gerya and Yuen, 2007; Golabek
et al., submitted for publication) and possible effects of phase
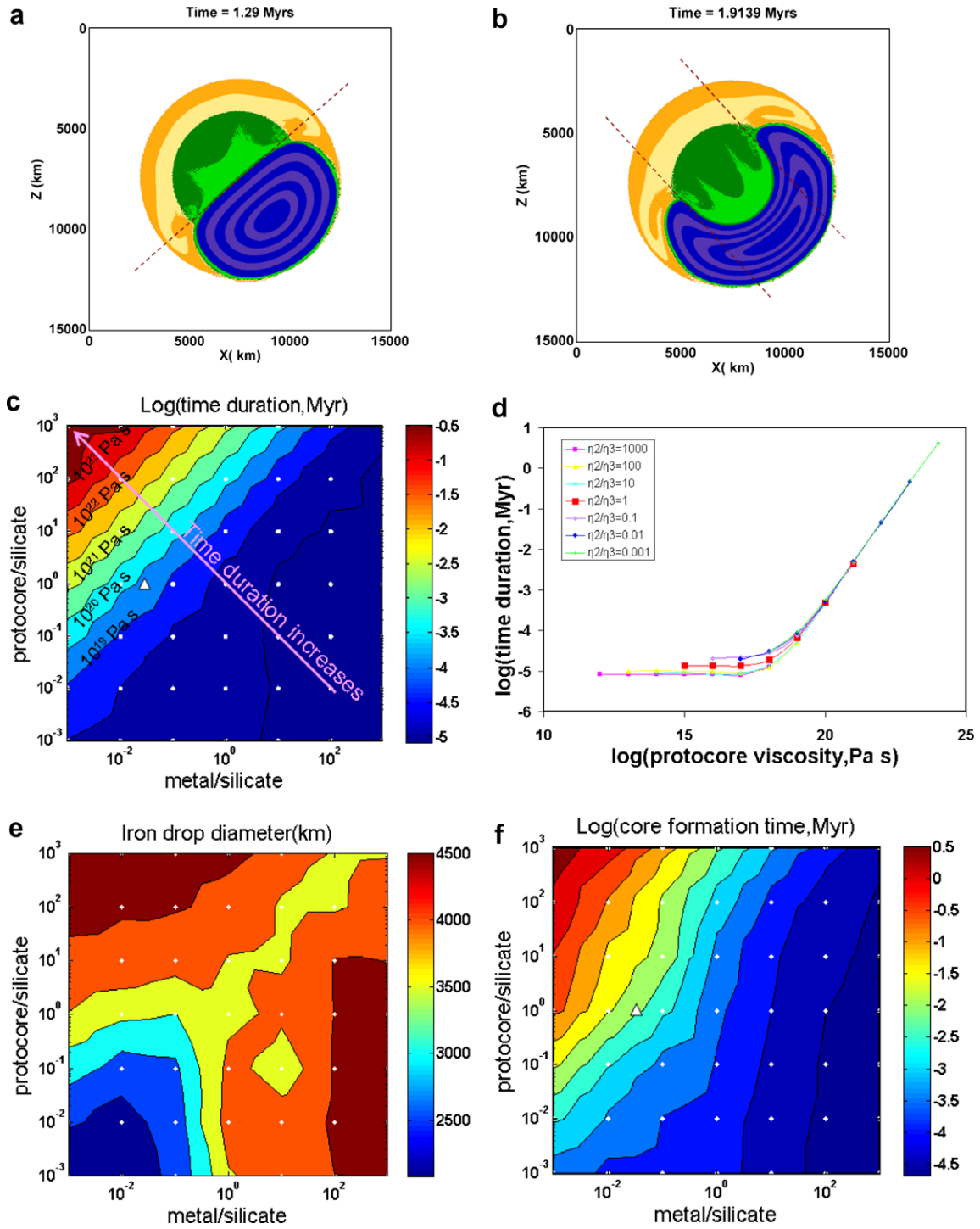
Fig. 12. Numerical results for the protocore deformation and metallic core formation timescales computed for Earth-sized bodies (tests1–49 in Table 1): (a) and (b) Two reference stages taken for evaluating the duration of the protocore deformation. (c) Protocore deformation duration map derived from the time difference of two reference stages. (d) Protocore deformation duration as a function of protocore viscosity. (e) The size of the iron core measured for the second reference stage. (f) Metallic core formation time corresponding to the moment when ~80% of metal is located in the center of the protoplanet. White triangle shows conditions for numerical experiments of Honda et al. (1993).

transitions including metal/silicate melting processes are not taken into account. In nature planetary materials have strongly non-Newtonian pressure, temperature and stress-dependent rheology and are likely to be partially or fully molten due to the energy feedback from planetary accretion and core formation processes. Therefore further, more realistic numerical studies are needed for understanding core formation processes. Indeed, we believe that the numerical approach and conceptual direction outlined in this paper could serve as a tool box for more complex and realistic simulations.

5. Summary

We developed and tested an efficient 2D numerical methodology for modeling gravitational redistribution processes in a quasi spherical planetary body based on a simple Cartesian grid. This
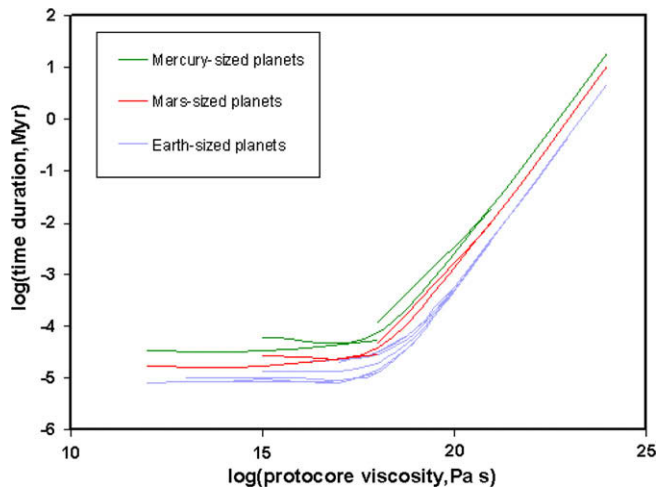
Fig. 13. Numerical results for the protocore deformation timescale (Fig. 12) as a function of the protocore viscosity and the bodies' size. The green color is for the Mercury-sized, the red is for Mars-sized, the blue is for Earth-sized protoplanets. (For interpretation of the references to color in this figure legend, the reader is referred to the web version of this article.)

methodology allows one to implement large viscosity contrasts and to handle properly a free surface and self-gravitation. With this novel method we investigated in a simplified way possible modes of internal reshaping resulting from gravitationally unstable global three-layer structures in the interiors of large metal–silicate planetary embryos as suggested by previous models on cold accretion. Results of our experiments show that the viscosity structure of the planetary body is an important factor controlling the geometrical mode of reshaping. The aspherical deviation of the bodies' shape and the exposure of the protocore occur during the core formation process with high viscosity ratios of protocore to silicate and metal to silicate. The free planetary surface condition we have applied does indeed exert a significant influence on the reshaping process of core formation and allows the capture of transient aspherical deviations of the body geometry. This process will convert a large amount of potential energy into temperature, and causes strongly non-uniform depths of the magma ocean around the protoplanet. The limited amount of metal–silicate equilibration on such protoplanets should also have geochemical implications for the terrestrial planets, which may partly accrete these bodies from the Asteroid belt.

Our simplified model also predicts that the time for metallic core formation out of the metal-rich layer depends mainly on the dynamics of the deformation of the solid strong protocore. In nature this dynamics will be strongly dependent on the effective viscosity of the protocore, which should generally have non-Newtonian pressure-, temperature-, and stress-dependent rheology with strong thermomechanical feedbacks from gravitational energy dissipation (Gerya and Yuen, 2007). Therefore the modes of reshaping and chemical equilibration may change in space and time and further studies are needed to investigate rheological controls of protocore deformation dynamics.

Acknowledgments

References

Asahara, Y., Frost, D.J., Rubie, D.C., 2007. Partitioning of FeO between magnesiowüstite and liquid iron at high pressures and temperatures: Implications for the composition of the Earth's outer core. Earth Planet. Sci. Lett. 257, 435–449.

Chambers, J.E., 2004. Planetary accretion in the inner Solar System. Earth Planet. Sci. Lett. 223, 241–252.

Chambers, J.E., Wetherill, G.W., 1998. Making the terrestrial planets: N-body integrations of planetary embryos in three dimensions. Icarus 136, 304–327.

Chambers, J.E., Wetherill, G.W., 2001. Planets in the Asteroid belt. Meteorit. Planet. Sci. 36, 381–399.

Elsasser, W.M., 1963. Early history of the Earth. In: Geiss, J., Goldberg, E. (Eds.), Earth Science and Meteorites, North Holland, Amsterdam, pp. 1–30.

Gerya, T.V., Yuen, D.A., 2007. Robust characteristics method for modeling multiphase visco-elasto-plastic thermo-mechanical problems. Phys. Earth Planet. Inter. 163, 83–105.

Golabek, G.J., Schmeling, H., Tackley, P.J., 2008. Earth's core formation aided by flow channelling instabilities induced by iron diapirs. Earth Planet. Sci. Lett. 271, 24–33.

Golabek, G.J., Gerya, T.V., Kaus, B.J.P., Ziethe, R., Tackley, P.J., submitted for publication. Rheological controls on the terrestrial core formation mechanism. Geochem. Geophys. Geosyst.

Grimm, R.E., McSween, H.Y., 1993. Heliocentric zoning of the asteroid belt by aluminum-26 heating. Science 259, 653–655.

Höink, T., Schmalzl, J., Hansen, U. 2006. Dynamics of metal-silicate separation in a terrestrial magma ocean. Geochem. Geophys. Geosyst. 7, Q09008. doi: 10.1029/2006GC001268.

Honda, R., Mizutani, H., Yamamoto, T., 1993. Numerical simulation of Earth's core formation. J. Geophys. Res. 98, 2075–2089.

Ida, S., Nakagawa, Y., Nakazawa, K., 1987. The Earth's core formation due to Rayleigh–Taylor instability. Icarus 69, 239–248.

Ida, S., Nakagawa, Y., Nakazawa, K., 1989. The Rayleigh–Taylor instability in a self gravitating two-layer fluid sphere. Earth Moon Planets 44, 149–174.

Karato, S., Murthy, V.R., 1997. Core formation and chemical equilibrium in the Earth–I. Physical considerations. Phys. Earth Planet Interios 100, 61–79.

Melosh, H.J., 1990. Giant impacts and the thermal state of the early Earth. In: Newsom, H.E., Jones, J.H. (Eds.), Origin of the Earth. Oxford University Press, New York, pp. 69–83.

Merk, R., Breuer, D., Spohn, T., 2002. Numerical modeling of 26Al-induced radioactive melting of asteroids considering accretion. Icarus 159, 183–191.

O'Brien, D.P., Morbidelli, A., Bottke, W.F., 2007. The primordial excitation and clearing of the asteroid belt—Revisited. Icarus 191, 434–452.

Pollack, J.B., Hubickyj, O., Bodenheimer, P., Lissauer, J.J., Podolak, M., Greenzweig, Y., 1996. Formation of the giant planets by concurrent accretion of solids and gas. Icarus 124, 62–85.

Raymond, S.N., Quinn, T., Lunine, J.I., 2007. High-resolution simulations of the final assembly of Earth-like planets. 2. Water delivery and planetary habitability. Astrobiology 7, 66–84. doi:10.1089/ast.2006.06-0041.

Rubie, D.C., Melosh, H.J., Reid, J.E., Liebske, C., Righter, K., 2003. Mechanisms of metal–silicate equilibration in the terrestrial magma ocean. Earth Planet. Sci. Lett. 205, 239–255.

Rubie, D.C., Nimmo, F., Melosh, H.J., 2007. Formation of Earth's core. In: Schubert, G., Stevenson, D.J. (Eds.), Treatise on Geophysics, vol. 9. Elsevier, New York, pp. 51–90.

Samuel, H., Tackley, P.J., 2008. Dynamics of core formation and equilibration by negative diapirism. Geochem. Geophys. Geosyst. 9, Q06011. doi:10.1029/2007GC001896.

Sasaki, S., Nakazawa, K., 1986. Metal–silicate fractionation in the growing Earth: Energy source for the terrestrial magma ocean. J. Geophys. Res. 91, 9231–9238.

Schmeling, H., and 12 colleagues, 2008. A benchmark comparison of spontaneous subduction models – Towards a free surface. Phys. Earth Planet. Interiors, 7, 8–9. doi:10.1016/j.pepi.2008.06.028.

Senshu, H., Kuramoto, K., Matsui, T., 2002. Thermal evolution of a growing Mars. J. Geophys. Res. 107 (E12), 5118. doi:10.1029/2001JE001819.

Solomatov, V.S., 2000. Fluid dynamics of a terrestrial magma ocean. In: Canup, R., Righter, K. (Eds.), Origin of the Earth and Moon. Univ. of Arizona Press, Tucson, pp. 323–338.

Stevenson, D.J., 1981. Models of the Earth's core. Science 214, 611–619.

Stevenson, D.J., 2008. A planetary perspective on the deep Earth. Nature 451, 261–265.

Wetherill, G.W., 1990. Formation of the Earth. Annu. Rev. Earth Planet. Sci. 18, 205–256.

Wetherill, G.W., 1992. An alternative model for the formation of the asteroids. Icarus 100, 307–325.